# Spin-state Switching and Single-molecule Conductance Studies of Iron(II) Complexes Composed of Functional 2,6-bis(pyrazol-1-yl)pyridine-based Ligands

Senthil Kumar Kuppusamy,*[a] Sebastiaan van der Poel,[b] Sören Schlittenhardt,[c] Olaf Fuhr,[c,d] Herre S. J. van der Zant,[b] and Mario Ruben [a,c,e]

[a]Institute of Quantum Materials and Technologies (IQMT),
Karlsruhe Institute of Technology (KIT),
Kaiserstraße 12,
76131, Karlsruhe, Germany.
E-mail : senthil.kuppusamy2@kit.edu

[b]Kavli Institute of Nanoscience,
Delft University of Technology,
PO Box 5046, 2600 GA Delft,
The Netherlands.

[c]Institute of Nanotechnology (INT),
Karlsruhe Institute of Technology (KIT),
Kaiserstraße 12,
76131, Karlsruhe, Germany.

[d]Karlsruhe Nano Micro Facility (KNMFi),
Karlsruhe Institute of Technology (KIT),
Kaiserstraße 12,
76131, Karlsruhe, Germany.

[e]Centre Européen de Sciences Quantiques (CESQ)
Institut de Science et d'Ingénierie, Supramoléculaires (ISIS),
8 allée Gaspard Monge, BP 70028,
67083 Strasbourg Cedex, France.

## Abstract

Iron(II)-based spin-crossover (SCO) complexes are promising candidates for several applications—for example, as switching and memory elements in molecule-based information processing architectures. Consequently, the spin-state switching characteristics of such complexes have been studied at the bulk, thin-film, and single-molecule levels. In an effort to link the bulk and single-molecule switching regimes, we have studied three mononuclear iron(II) complexes composed of 2,6-bis(pyrazol-1-yl)pyridine (BPP)-based ligands **L$^1$**-**L$^3$**. Complex **1**—[Fe(**L$^1$**)$_2$](BF$_4$)$_2$·CH$_3$CN—underwent bistable spin-state switching with a transition temperature ($T_{1/2}$) of 253 K and a thermal hysteresis width ($\Delta T_{1/2}$) of 5 K. Complex **2**—[Fe(**L$^2$**)$_2$](BF$_4$)$_2$·CH$_3$CN—showed two-step bistable switching—$T_{1/2}$ = 258 K (step 1) and 206 K (step 2)—with wide $\Delta T_{1/2}$—40 K (step 1) and 56 K (step 2)—at a scan rate of 0.25 K/min. Remarkably, widening of $\Delta T_{1/2}$ with slow scan rates, below 1 K/min, is noted for **2**. In contrast, **3**—[Fe(**L$^3$**)$_2$](BF$_4$)$_2$·2CH$_3$CN—showed lattice-solvent-dependent spin-state switching; loss of lattice solvent resulted in a high spin (HS) phase that underwent gradual and incomplete

switching. Single-molecule transport studies of **2** and **3** functionalized with thiomethyl (SMe) anchoring groups indicate charge transport through segments of the molecules attributed to the partially stretched configurations of the complexes in the junctions.

## 1. Introduction

Spin-crossover (SCO) has a long-standing history and remains a subject of contemporary interest and relevance.[1–11] The phenomenon is one of the pillars of molecular magnetism[12] and applications, for example, in the domains of switching, memory, molecular electronics, and molecular spintronics have been proposed.[13–15] Iron(II) complexes composed of nitrogen donor ligands featuring moderate ligand field strength constitute the major body of the SCO studies.[16–20] The interest in iron(II) complexes stems from the fact that the low spin (LS) form of the complexes is diamagnetic due to the paring of all electrons in the $t_{2g}$ level ($d^6$; $t_{2g}^6$, $e_g^0$). This allows for a reversible spin-state interconversion between diamagnetic LS and paramagnetic high spin (HS—$d^6$; $t_{2g}^4$, $e_g^2$) states.

The SCO phenomenon has been studied in the solution and solid states, as well as in the thin-film and single-molecule levels. In the solution state, spin-state switching is studied by subjecting a sample to a temperature[21–23] or light stimulus.[24–27] The light-induced spin-state switching of 2,2'-bipyridine (bpy)-based iron(II) complexes—$[Fe(bpy)_3]^{2+}$—in solution is a single-molecular phenomenon, and ultrafast photo-induced spin-state switching, as a consequence of an unusually fast intersystem crossing rates, has been observed.[28–31] In the solid- and thin-film states, SCO is studied by predominantly employing temperature and light stimuli.[32–37] Intermolecular interactions play a strong role in determining the switching characteristic in the solid- and thin-film states and spin-state switching leads to changes in magnetic moment, conductance variation, and photophysical properties.[38–41] Stimuli such as mechanical stretching and external electric fields have been leveraged to induce spin-state switching at the single-molecule level.[42–48] Spin-phonon coupling mediated stochastic spin-state switching has also been observed at the single-molecule level.[49,50] In the absence of intermolecular interactions, the switching and the consequent conductance variation is mainly determined by the electronic structure of the molecule and electrode-molecule interactions.

The above discussion makes it clear that spin-state switching can be studied across various levels—from the bulk to the single-molecule level—with significant implications for both fundamental understanding of the switching process and practical applications. For example, bulk state switching studies coupled with crystallographic investigations[51–53] enable one to understand mechanisms governing bi-stable switching with wide thermal hysteresis width ($\Delta T$), useful for realizing SCO-based memory applications.[54,55] On the other hand, the utility of a molecule as a molecular-electronics or -spintronics module relies on the spin-state-dependent conductance variation in single-molecule junctions.[56,57] Studies of spin-state switching of thin-films supported on substrates remain at the interface between bulk and single-molecule level. In the thin-film state, the nature of interaction between molecule and substrate—termed spinterface—plays a crucial role in the few mono-layers thick regime. Whereas, intermolecular interactions dominate the switching process in thick films.[58,59]

The key message here is spin-state switching studies of the same complex in all three levels—bulk, thin-film, and single-molecule—could unveil distinct facets of the phenomenon, as

discussed above. However, such comprehensive investigations have so far been carried out for only a limited number of molecules. Prominent examples are the prototypical $[Fe(phen)_2(NCS)_2]$ (phen = 1,10-phenanthroline)[60,61] and $[Fe(H_2Bpz_2)_2(L)]$ ($H_2Bpz_2$ = dihydrobis(pyrazol-1-yl)borate; L = 2,2'-bipyridine or 1,10-phenanthroline) complexes.[32,47,62,63] The limited number of such studies emphasizes the need to expand the SCO molecular toolkit to deepen our fundamental understanding of the phenomenon and harness the related applications. To address the issue, we have studied the spin-state switching characteristics of supramolecular iron(II) complexes in the bulk state and performed transport studies at the single-molecule level.[64] In this contribution, we report on the spin-state switching and single-molecule transport characteristic of a series of iron(II) complexes—**1-3** (Figure 1)—composed of BPP-based (BPP = 2,6-bis(pyrazol-1-yl)pyridine) ligands. Complex **1** is composed of a novel BPP ligand (**L$^1$**), featuring no anchoring group for metallic electrodes. The complex is designed as a basic unit to study the spin-state switching in the bulk state and make comparisons with its thiomethyl (SMe) anchoring group bearing counterparts—complexes **2** and **3**—composed of BPP-based ligands **L$^2$** and **L$^3$**, respectively.

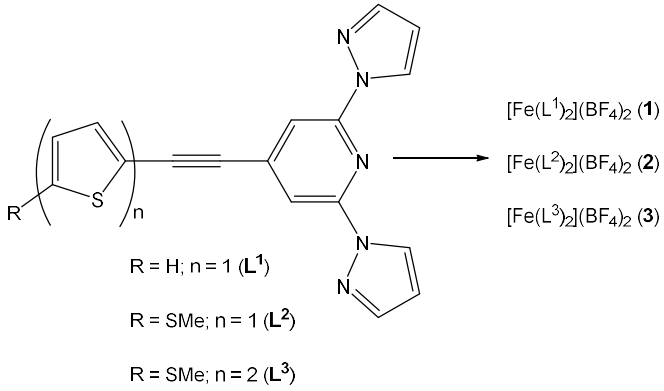


**Figure 1.** Molecular structures of ligands **L$^1$**, **L$^2$**, and **L$^3$** used to prepare the corresponding iron(II) complexes **1**, **2**, and **3**.

In the following sections, the SCO characteristics of the complexes **1-3** in the bulk crystalline solid-state and transport studies of complexes **2** and **3** at the single-molecule level are presented.

## 2. Results and Discussion

### 2.1 Synthesis of the Ligands and Complexes and Thermogravimetric Analysis of the Complexes

The ligands **L$^1$**, **L$^2$**, and **L$^3$** have been synthesized employing the Sonogashira coupling reaction[65] between the corresponding ethynyl precursor (1, 2, or 3) and 4-iodo-2,6-di(1H-pyrazol-1-yl)pyridine (I-BPP; 4) as shown in scheme 1. The I-BPP starting material was prepared utilizing a diazotization-iodination reaction sequence reported by Krasnokutskaya et al.[66] The reaction can be performed using the commonly available laboratory reagents in acetonitrile, serving as a facile route to prepare I-BPP, a useful starting material for the preparation of BPP derivatives.[64,67–69] Treatment of solid $[Fe(BF_4)_2]\cdot 6H_2O$ with pale-yellow acetonitrile solution of the ligands at room temperature (RT) yielded red-orange solutions, indicating complex formation. Slow diffusion of diethyl ether into acetonitrile solutions of the

complexes at 278 K resulted in the formation of X-ray quality single crystals. See section S3 of supporting information for more details.

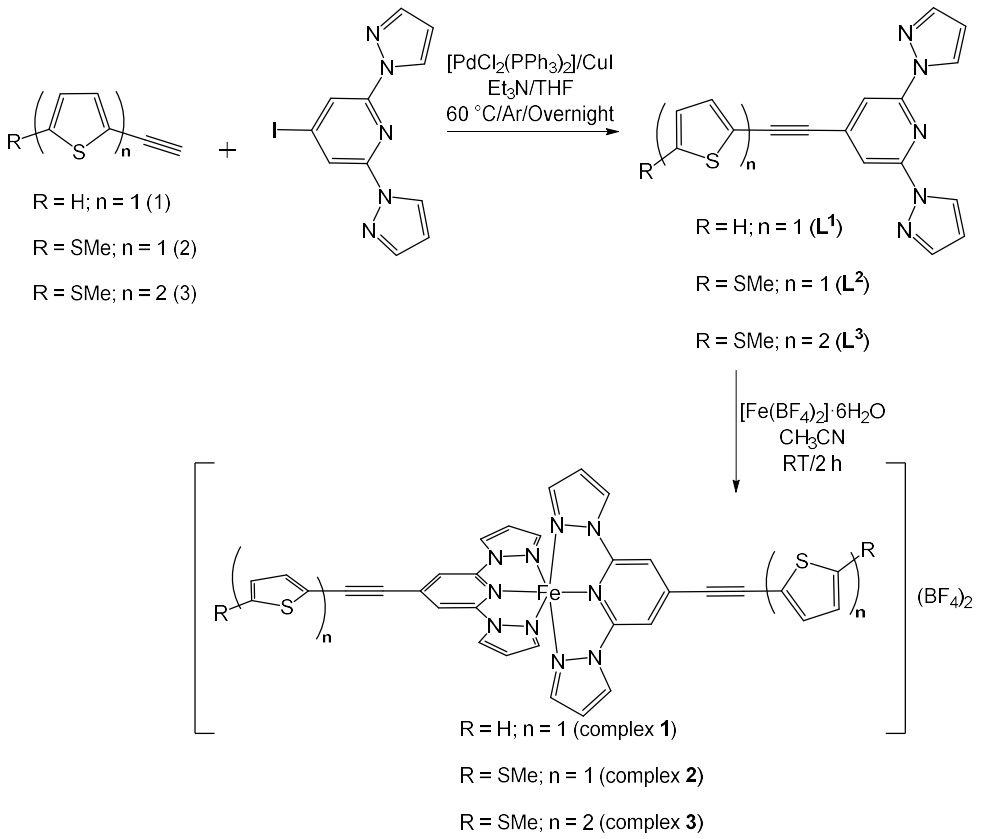


**Scheme 1.** Synthesis of the ligands and complexes. Sonogashira coupling of the ethynyl precursors with I-BPP yielded the ligands in moderate yields. Treatment of $[Fe(BF_4)_2]\cdot 6H_2O$ with acetonitrile solutions of the ligands followed by isothermal diffusion of diethyl ether resulted in the formation of crystalline complexes **1**, **2**, and **3**.

Thermogravimetric analysis (TGA) of the crystalline forms of complexes **1** and **2** (see section 2.2) under nitrogen atmosphere revealed a complete loss of lattice acetonitrile solvent at 398 K (125 °C) and 401 K (128 °C), respectively (Figures S10 and 11). For complex **3**, a partial loss of the lattice solvent (Figure S12) is observed at 435 K (162 °C). See Table S3 for additional information.

### 2.2 Molecular Structures of Complexes 1, 2, and 3 Obtained from Single-crystal X-ray Diffraction Studies

The molecular structures of the complexes obtained from single-crystal X-ray diffraction (SC-XRD) studies are depicted in Figure 2. Structures of complex **1** in the HS and LS states can be determined at 300 K and 150 K, respectively. The HS and LS forms of the complexes crystallized in the *C*2/*c* space group belonging to the monoclinic crystal system. Complexes **2** and **3** crystallized in the P-*1* space group belonging to the triclinic crystal system. Complexes **1** and **2** crystallized with one lattice acetonitrile molecule, whereas complex **3** crystallized with two lattice acetonitrile molecules.

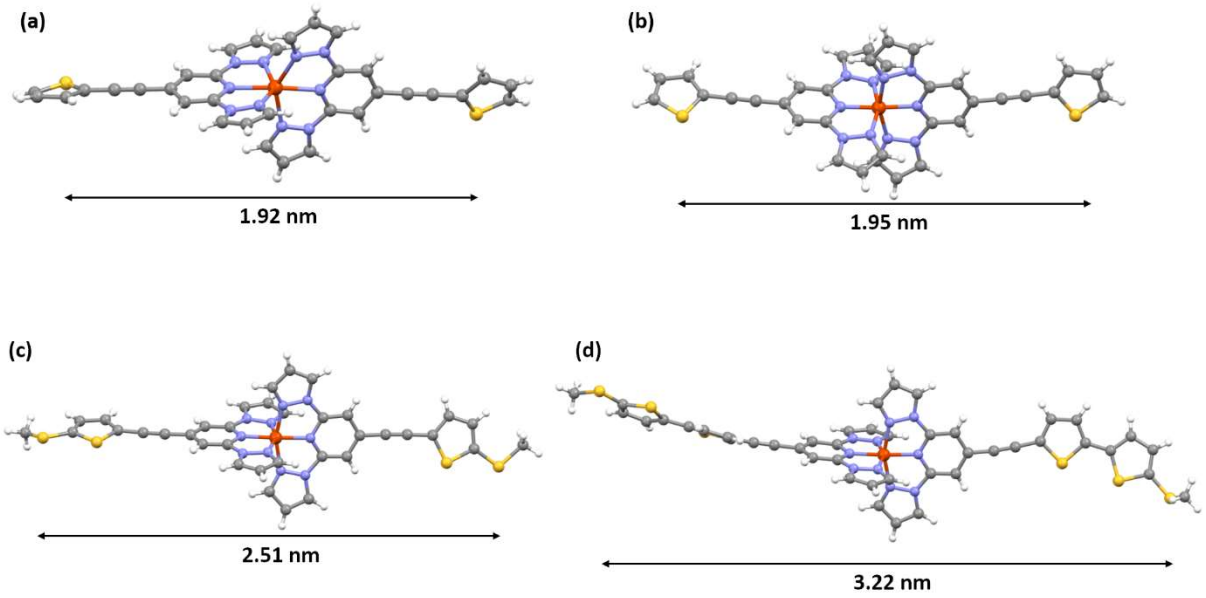


**Figure 2.** Molecular structures of complexes **1-3** obtained from single-crystal X-ray diffraction (SC-XRD) studies. Structures of complex **1** in the (a) high spin and (b) low spin states and complexes (c) **2** and (d) **3** in the low spin state. The values below the arrows represent the end-to-end distances measured between the outermost sulphur atoms; S atoms of the thiophene ring in complex **1** and S atoms of the thiomethyl groups in complexes **2** and **3**.

Spin-state switching involves structural variation. An easily discernible one is the change in the metal-ligand bond length, which is longer for the HS state relative to the LS state, as depicted in Table 1 for complex **1**. Spin state switching in BPP-based iron(II) complexes often result in change in angular parameters.[70] The trans-N{pyridine}-Fe-N{pyridine}angle ($\phi$); N{pyrazole}-Fe-N{pyrazole} clamp angle ($\psi$); angle between the planes of the two ligands ($\vartheta$); average value of four cis-N{pyridyl}-Fe-N{pyrazole}angles ($\alpha$) all vary between the LS and HS structures. The angles $\phi$ and $\vartheta$ represent the degree of distortion; complexes having ideal octahedral geometry feature $\phi$ = 180° and $\vartheta$ = 90°. The geometrical distortion of a complex from an ideal octahedral geometry is represented by the distortion index ($\Sigma$), which is calculated using the relation $\sum_{i=1}^{i=12} = |90 - i|$, where i is one of the twelve cis-N-Fe-N angles. The parameter $\Theta$ indicates the geometrical distortion of a coordination polyhedron from ideal octahedral geometry to trigonal prismatic geometry. The parameters $\Sigma$ and $\Theta$ are zero for ideal octahedral geometry.

The successful structural determination of complex **1** in the LS and HS states allowed us to compare the bond lengths and angular parameters between the two spin isomers, as tabulated in Table 1. The corresponding values for the LS structures of complexes **2** and **3** are also collected in Table 1. The angular parameters are obtained using OctaDist software.[71]

**Table 1.** Average Fe-N bond lengths (Å), N-Fe-N bond angles (°), and angular parameters of complex **1** in the HS and LS states and complexes **2** and **3** in the LS state.

| Parameter | Complex | | | |
|---|---|---|---|---|
| | **1** (HS) | **1** (LS) | **2** (LS) | **3** (LS) |

| $T$/K | 300 | 150 | 160 | 120 |
|---|---|---|---|---|
| rFe-N(Average) | 2.1524 | 1.9449 | 1.9432 | 1.9438 |
| Npyri-$Fe_1$-Npyri ($\phi$) | 163.82 | 176.18 | 174.70 | 176.90 |
| Npyra-$Fe_1$-Npyra ($\psi$) | 144.26 | 159.83 | 160.44 | 160.31 |
| Npyra-$Fe_1$-Npyra ($\psi$) | 144.26 | 159.83 | 160.43 | 159.87 |
| $\Sigma$ | 167.7176 | 94.5224 | 84.7969 | 86.4374 |
| $\vartheta$ | 76.63 | 80.71 | 87.54 | 88.28 |
| $\alpha$ | 72.92(5) | 80.06 | 80.27 | 80.09 |
| $\Theta$ | 637.4221 | 310.0871 | 299.6496 | 292.7377 |

The bond lengths and angular parameters obtained for the LS structures of complexes **2** and **3** are in the range reported for BPP-based iron(II) complexes.[70] The HS-to-LS spin-state switching of complex **1** is accompanied with structural variations, as reflected in the variation of angular parameters. The $\Delta\phi$ = 12.36° and $\Delta\vartheta$ = 4.08° obtained for the complex indicate strong structural variation upon spin-state switching. The $\Delta\Theta$ = 327.33° and $\Delta\Sigma$ = 73.19° indicate a pronounced deviation from an ideal octahedral geometry to a trigonal prismatic one upon LS to HS switching. The parameters compiled in Table 1 for the complexes can be used to ascertain the role of structural parameters on the nature of spin-state switching associated with the complexes, especially for complex **1**, as discussed below.

### 2.3 Spin-state Switching Characteristics of Complexes 1-3

Crystals obtained from two different batches (batch 1 and 2) were used to check for the reproducibility of the crystallization process and the spin-state switching characteristic of complex **1**. At 300 K, complex **1**, obtained from batch 1, showed a $\chi T$ value of 3.48 $cm^3K\ mol^{-1}$ indicating the HS state of the complex (Figure 3). Cooling (cycle 1) the complex at a scan rate of 5 K/min caused an abrupt HS to LS switching in the 250 K to 240 K temperature range. Further cooling resulted in a gradual HS to LS switching until 119 K. Below 119 K, a LS-phase with $\chi T$ = 0.007 $cm^3K\ mol^{-1}$ (5 K) was obtained. Heating (cycle 1) the complex from 5 K resulted in the overlap of the heating and cooling branches until 245 K. Unlike the cooling branch, the gradual switching was maintained until 251 K. Further heating induced an abrupt LS to HS switching, the HS phase was attained at 265 K. Overall, a $T_{1/2}$ = 252.5 K and $\Delta T_{1/2}$ = 5 K were observed for complex **1** at the scan rate of 5 K/min. A similar SCO profile was observed for the second cool-heat cycle performed at a 5 K/min scan rate. To get insight into the scan rate dependence of the spin-state switching, a third cycle was performed at a scan rate of 1 K/min. While the HS-to-LS switching profiles obtained in the cycles 1-2 and cycle 3 are comparable, the LS to HS switching branches measured at those scan rates are incomparable. The switching

in the LS to HS branch at 1 K/min is a two-step process, as depicted in the inset of Figure 3b; thermal hysteresis widths of 9 K ($T_{1/2}$ = 254.5 K) and 19 K ($T_{1/2}$ = 259.5 K) were obtained for the first and second steps, respectively. Moreover, $\chi T$ = 3.214 cm$^3$ K mol$^{-1}$ at 300 K was obtained for the LS to HS branch measured at the scan rate of 1 K/min. The value is smaller than the one observed for the HS-phase obtained in cycles 1 and 2. Such $\chi T$ reduction upon repeated cycling is attributed to the switching-induced fatigue and the consequent cracking of the crystals, possibly accompanied by the lattice solvent loss. Further scan rate-dependent studies were not performed due to the crystal cracking inferred from the experiments.

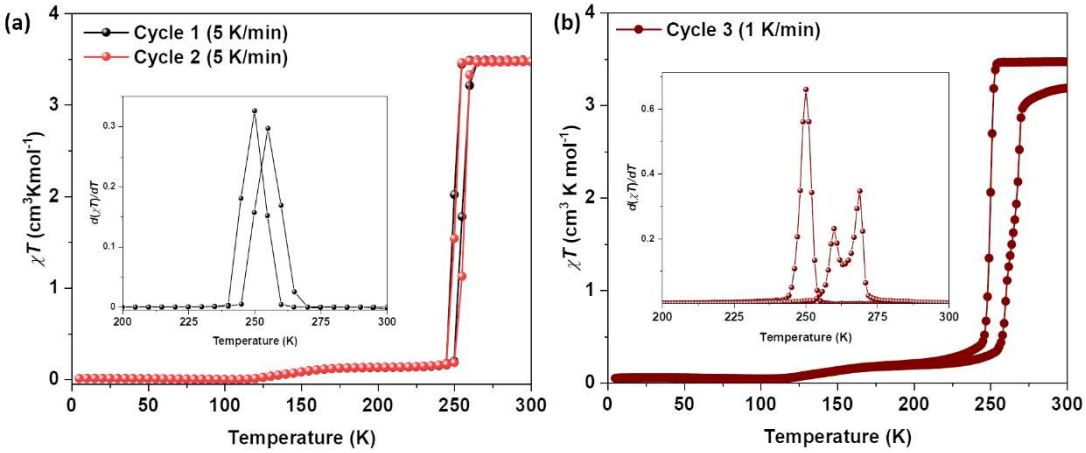


**Figure 3.** Spin-state switching characteristics of complex **1**. (a) $\chi T$ versus $T$ plots showing spin-state switching observed in cycles 1 and 2, measurements were performed at a scan rate of 5 K/min. (b) SCO characteristics of the complex observed in cycle 3 measured at a scan rate of 1 K/min.

Crystals of the complex obtained from batch 2 (cycle 1, scan rate = 5 K/min) showed a similar spin-state switching characteristic (Figure S13) as the one obtained for the batch 1, albeit with marked differences. The gradual spin-state switching phase observed in batch 1 is not observed in batch 2. A relatively higher $T_{1/2}$ = 255 K and wider $\Delta T_{1/2}$ = 11 K were observed for the crystals obtained from batch 2 than the ones observed for batch 1. To test the effect of lattice solvent removal on the SCO characteristics, the crystals obtained in batch 2 were heated at 398 K under vacuum overnight. The solvent-free sample showed $\chi T$ = 2.78 cm$^3$ K mol$^{-1}$ at 300 K indicating a mixed phase composed of HS and LS states (Figure S14). No meaningful SCO was observed upon cooling. Overall, the results presented above elucidate that the complex experiences a change in crystallinity upon repeated cycling with consequent changes in the spin-state switching characteristics. Additionally, slight variations in the switching parameters observed between the batches could be attributed to minor differences in the grinding of the crystals performed prior to the magnetic measurements and crystallization process.

To assess the SCO characteristics, complex **2** was centred at 300 K (Figure 4) and data were collected in the cooling mode until 5 K (cycle 1; first cooling), employing a scan rate of 5 K/min. At 300 K, $\chi T$ product of 0.85 cm$^3$ K mol$^{-1}$ was obtained. The value gradually decreased upon cooling and at 5 K, $\chi T$ = 0.04 cm$^3$ K mol$^{-1}$ was obtained, indicating the LS state of the complex.

Upon subsequent heating (cycle 1; first heating), a gradual and complete SCO occurred. $\chi T$ = 3.22 $cm^3$ K $mol^{-1}$ at 350 K and $T_{1/2}$ = 335 K were estimated from the heating branch (Figures 4 and S15-16).

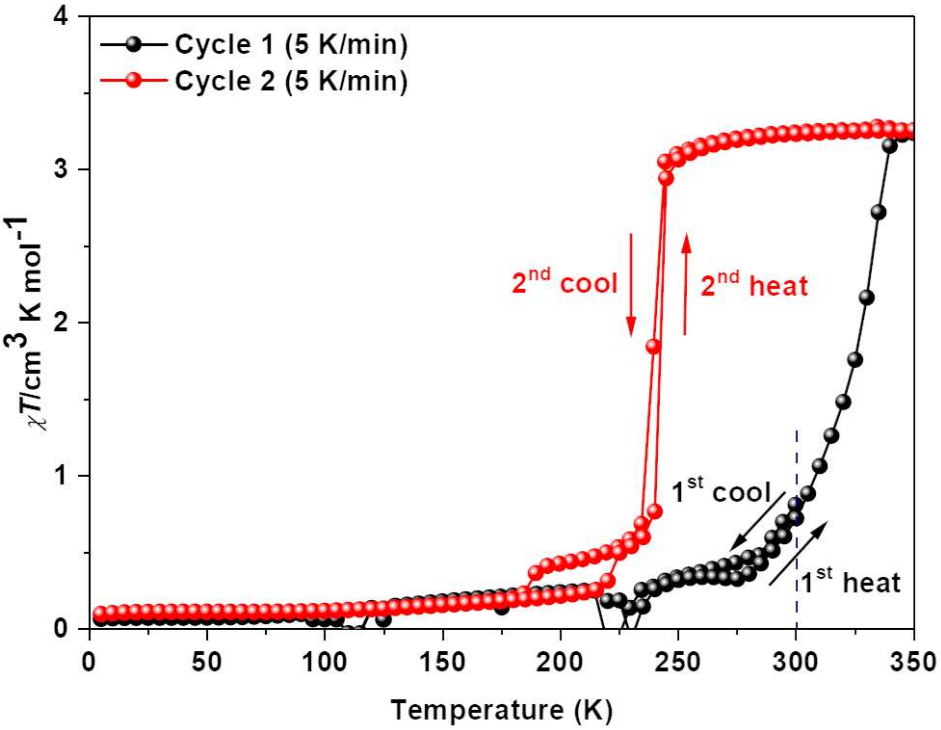


**Figure 4.** Spin-state switching characteristics of complex **2.** The $\chi T$ versus $T$ plots of the complex obtained in cycles 1 and 2. The blue dotted line indicate the temperature (300 K) at which the sample was centered and data collection started in the cooling mode, denoted as $1^{st}$ cool.

In the second cycle, cooling the sample from 350 K to 5 K (second cooling, scan rate = 5 K/min; Figure 4) resulted in the shifting of the HS to LS switching branch well-below 300 K. Remarkably, the switching became abrupt and a plateau-like region encompassing 225 K to 185 K region was observed, implying an intermediate spin phase (ISP) predominantly composed of the LS state. Cooling below 185 K resulted in the switching of the remnant HS fraction, and at 5 K, a $\chi T$ value of 0.09 $cm^3 mol^{-1}$ K was obtained, indicating the LS state of the complex. Upon heating (cycle 2; second heating), the LS to HS switching occurred at a relatively higher temperature in the plateau region than the one observed in the cooling branch, culminating as the formation of a 32 K wide thermal hysteresis width. Further heating resulted in an abrupt LS to HS switching of the remaining LS complexes. A small thermal hysteresis width of about 1 K was observed in the abrupt switching region. See S16 for a $\delta\chi T/\delta T$ plot showing transition temperatures of the cooling and heating branches of cycle 2. Overall, in cycle two, a two-step spin-state switching was observed for complex **2** with the following switching parameters: $T_{1/2}$ = 239 K; $\Delta T$ = 1 K (first step, abrupt region) and $T_{1/2}$ = 204 K; $\Delta T$ = 32 K (second step, plateau region). A subsequent cycle (cycle 3; Figure 5a) performed at 5K/min yielded comparable spin-state switching characteristics with the ones observed in cycle 2 (Table 2).

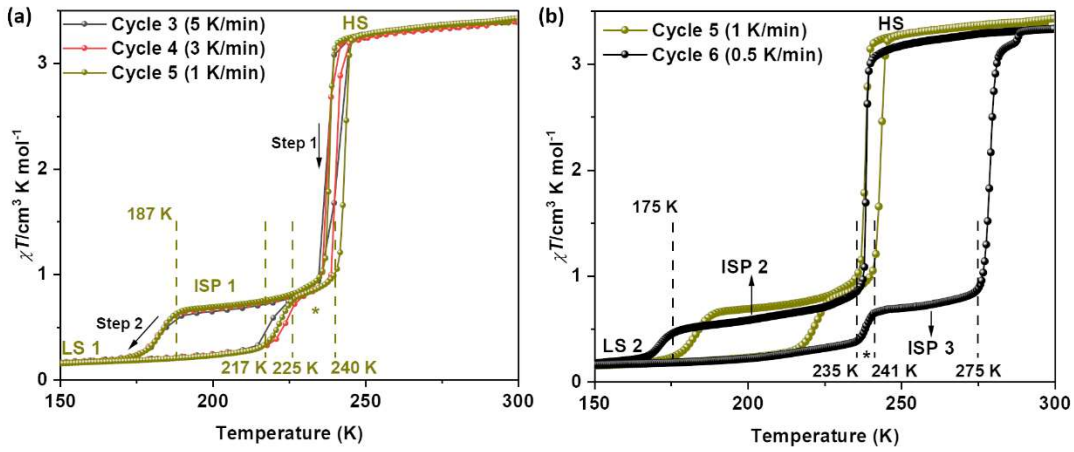


**Figure 5.** Spin-state switching characteristics of complex **2.** (a) $\chi T$ versus $T$ plots of the complex obtained from cycles 3, 4, and 5. (b) Scan rate-dependent SCO characteristic of the complex observed in cycles 5 and 6.

To shed light on the scan-rate-dependent nature of the SCO associated with complex **2**, cool-heat cycles were performed employing scan rates of 3 K/min (cycle 4) and 1 K/min (cycle 5), as shown in Figure 5a. The spin-state switching characteristics observed in the cycles 4 and 5 are comparable with the ones observed in cycle 3, albeit with small variations in switching temperature and thermal hysteresis width, as collected in Table 2. The switching process observed in cycles 3-5 are summarized as follows. The cooling of the HS phase (Figure 5a) resulted in an abrupt and partial HS to LS switching (Step 1) with an onset of 240 K. Below 225 K, an intermediate spin phase, labelled as ISP1 in Figure 5a, is formed. The ISP1 underwent a gradual spin-state switching (Step 2) upon cooling with an onset of 187 K and a complete LS state—LS1 in Figure 5a—is observed below 175 K. Upon heating, the LS1 persisted until 217 K followed by a gradual switching. At 225 K, the cooling and heating traces coincided. After a 15 K thermal window, marked by * in Figure 5a, where a gradual switching is observed, abrupt spin-state switching ensued and the initial HS state is reached. See Figure 17a for the $\delta\chi T/\delta T$ plot showing the switching temperatures associated with each step in the cooling and heating branches of cycle 5.

**Table 2.** Parameters associated with the scan-rate-dependent spin-state switching characteristic of complex **2**.

| Cycle | Scan rate (K/min) | $T_{1/2}$ (K) | | $\Delta T$ (K) | |
|---|---|---|---|---|---|
| | | Step 1 | Step 2 | Step 1 | Step 2 |
| 2 | 5 | 239.5 | 204 | 1 | 32 |
| 3 | 5 | 239 | 201 | 2 | 38 |
| 4 | 3 | 240 | 203 | 4 | 42 |
| 5 | 1 | 241 | 203 | 6 | 40 |
| 6 | 0.5 | 258 | 204 | 41 | 67 |
| 7 | 0.25 | 258 | 206 | 40 | 56 |

In a nutshell, a two-step SCO with comparable switching profiles have been observed for cycles 2-5. The small yet noticeable variations in the switching parameters, especially *ΔT*, indicate evolution of lattice structure with scan rate. Such variation is attributed to the possible fatigue and continuous variation of the crystalline lattice upon repeated cycling, previously observed for a BPP-based iron(II) complex showing bi-stable spin-state switching.[72]

Spin-state switching is sensitive to scan rate (SR) and its desirable to study the switching process employing small SRs, especially when thermal hysteresis is observed.[34] In order to study the switching process of complex **2** at small SRs, we have performed a cool-heat cycle employing SR = 0.5 K/min. Upon comparing with the profile obtained at SR= 1 K/min, we observed a new intermediate spin phase, denoted as ISP2 in Figure 5b. The switching of ISP2 commenced 175 K and a new LS phase (LS2) is produced. A noticeable switching of the LS2 happened in the 235 K to 241 K region (marked with * in Figure 5b) and a new intermediate spin phase (ISP3) is reached. The onset of abrupt switching of the ISP3 is observed at 275 K and the HS state is reached at 289 K. As shown in Figure 5b, the switching the ISP2 occurs at a lower temperature relative to the one observed for ISP1. Upon heating, the ISP2 transitioned at a relatively higher temperature when compared with ISP1. Remarkably, in both the cooling and heating branches smaller scan rate—0.5 K/min versus 1 K/min—resulted in wider thermal hysteresis width. Additionally, the onset temperatures in the cooling and heating branches are shifted to lower and higher temperatures, respectively, for SR = 0.5 K/min relative to the temperatures observed for the SR = 1 K/min (Figure 5b). We have performed a subsequent cycle with a scan rate of 0.25 K—cycle 7 (Figure 6a) and observed comparable switching profiles for cycles 6 and 7 (Figure S17b). Such observation indicates that the switching process is reversible upon moving from SR = 0.5 K/min to 0.25 K/min. As in the cycles 2-5, we do note a variation of *ΔT* for the second step in cycles 6 and 7 (Table 2), this is attributed to small variations in lattice parameters upon repeated cycling.

To check if *ΔT* can be reversibly modulated by varying the scan rate, we have performed scan 8 with 5 K/min scan rate and noted that the wide hysteresis in the abrupt region remained as in cycle 7 (Figure 6b). Interestingly, employing a faster 10 K/min scan rate (cycle 9, Figure 6b) reversed the switching profile to the ones observed in cycles 3-5. A subsequent cycle performed employing a scan rate of 1 K/min yielded a different heating profile, relative to scan 9, with a new step above 260 K. These facets indicate that the thermal hysteresis width can be reversibly tuned by varying scan rate—cycle 5 versus cycle 6/7 versus cycle 9. However, our observations suggest that such reversibility can't be sustained for indefinite number of scans, most likely due to the gradual changes in the crystal lattice during repeated cycling. These changes may alter the intermolecular interactions and cause varying switching behaviour—as observed for complex **2** in cycles 9 and 10 and for a BPP-based complex studied by some of us.[72]

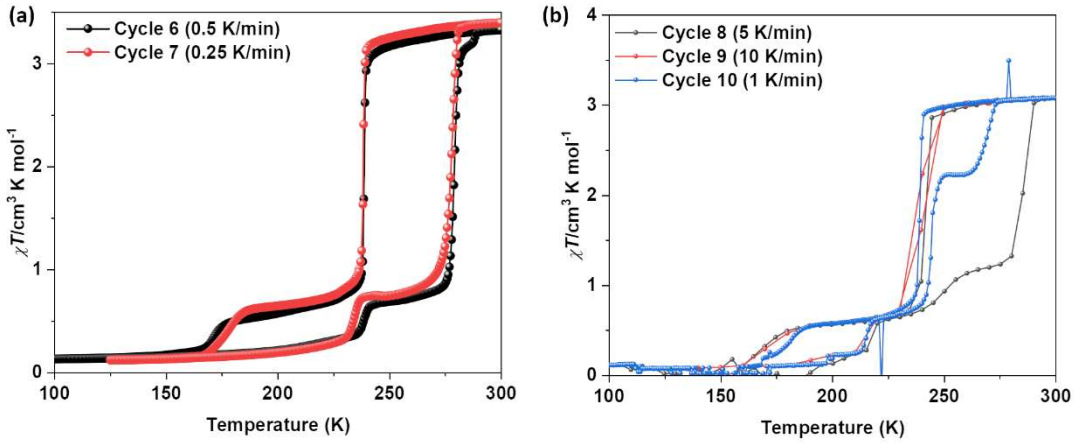


**Figure 6.** Spin-state switching characteristics of **2.** The $\chi T$ versus $T$ plots in (a) and (b) show the scan rate-dependent SCO characteristic of the complex.

To probe the structural aspects giving rise to the switching behaviour observed for **2** and to check for the reproducible nature of the switching between batches, we have prepared a fresh batch (batch 2) of crystals of 2. unfortunately, altogether different spin-state switching profiles were obtained for batch 2 (Figures S18) relative to the ones discussed above for batch 1. Prior to the measurements, we have checked the unit cell parameters of the crystals obtained from batch 2, and the values were found to be the same with the ones obtained for batch 1. Currently, the cause for the observation of two different spin-state switching profiles corresponding to the batches 1 and 2 of complex **2** remains unknown. The problem is more compounded due to the sluggish crystallization process and the concomitant precipitation of the ligand during the crystallization process.

To check for the role of lattice solvent molecule in controlling the SCO of complex **2**, the lattice solvent molecule was removed by heating the crystals obtained from batch 2 under high vacuum. The solvent-free sample showed incomplete and hysteretic SCO as depicted in Figure S19a. The partial HS to LS switching upon cooling proceeded in two steps; whereas, the partial LS to HS switching proceeded in three steps, and three different hysteresis widths ($\Delta T$) were obtained—8 K (step 1), 41 K (step 2), and 21 K (step 3), as inferred from the first derivative—$\delta\chi T/\delta T$—plots shown in Figure S19b. The switching profiles obtained at 5 K/min and 1 K/min scan rates are comparable.

Complex **3** showed lattice solvent-dependent spin-state switching characteristics, as depicted in Figure S20. Upon heating the sample from 5 K to 250 K (cycle 1; first heating), an almost linear $\chi T$ versus $T$ plot with $\chi T$ values in the range of 0.09 $cm^3$ K $mol^{-1}$ (5 K) to 0.27 $cm^3$ K $mol^{-1}$ (250 K) was observed, indicating the predominantly LS-state of the complex. Heating above 250 K led to the gradual LS to HS switching and around 400 K, $\chi T$ = 3.1 $cm^3$ K $mol^{-1}$ was observed, indicating the HS-state of the complex. A $T_{1/2}$ = 322 K was observed for the first heating branch. Subsequent cooling from 400 K to 50 K (cycle 1; first cooling) resulted in the occurrence of a very gradual HS to LS switching. A $\chi T$ = 2.16 $cm^3$ K $mol^{-1}$ was observed at 50 K. After that, a drop in the $\chi T$ product is observed, which is attributed to the depopulation of the excited levels of the zero-field split ground state term. A similar $\chi T$ versus $T$ plot was obtained in the subsequent heat-cool cycle (second cycle). The elemental analysis data of complex **3**

performed after the magnetic measurements indicated the complete loss of the lattice acetonitrile molecules, see section S3.4 of the SI. Based on this, the trapping of complex **3** in predominantly HS state and the gradual and incomplete HS to LS switching are attributed to the removal of lattice solvent after heating to 400 K.

### 2.4 Single-molecule Charge Transport Studies of Complexes 2 and 3

To investigate charge transport through complexes **2** and **3**, Mechanically Controlled Break-Junction (MCBJ) experiments were performed under ambient conditions using a home-built set-up.[73] The MCBJ technique entails the repeated breaking and fusing of a suspended gold nanowire on a flexible substrate using a three-point bending mechanism. In brief, the process starts off with a fully intact Au wire. Upon bending the substrate, the wire becomes increasingly thin, after which it will rupture to form two separate electrodes. During the breaking process a fixed DC bias voltage of 100 mV is applied between the source and drain, during which the conductance is continuously registered as a function of electrode separation distance. After rupture the electrodes are separated until the noise floor of the system is reached, whereafter the electrodes are fused and the breaking process can be repeated. Studying complexes **2** and **3** in the system is done by means of drop-casting a molecular solution of either complex **2** (concentration of 50 µM) or **3** (100 µM) in dichloromethane (DCM) onto the substrate containing the gold nanowire. Breaking traces are collected in a two-dimensional (2D) histogram, which is further analysed using clustering analyses using the clustering algorithm kmeans [74] (see SI S8.1 for more details).

The 2D conductance versus electrode separation distance histograms were constructed using 10000 consecutive breaking traces for both compounds **2** and **3** (see figure S22 for raw data). Figure 7 (a) and (b) show the molecular features of complexes **2** and **3** obtained from the clustering analysis. Here, we see similar slanted plateaus in case of the classes 1 and 2 of complex **2** and class 1 for complex **3**. A differently shaped class can be found for class 2, showing more elongated plateau reaching lower conductance levels. Both complexes **2** and **3** show the plateau-like feature in the range from $10^{-6}$ $G_0$ to $10^{-7}$ $G_0$ (1D histograms corresponding to the 2D histograms in Fig. 7 can be found in section S8.2, as well as the most probable conductance values for these features), in contrast to previously measured complexes with the same backbone and without SMe terminated linkers, which did not show clear molecular features.[64] Remarkably, the average trace lengths of the molecules sits between 0.9-1.1 nm for complex **2** and between 1.5-1.6 nm for complex **3** (see section S8.3 for average trace length histograms corresponding to 2D histograms as shown in Figure 7). Even after adding a snapback upon breaking of the wire between electrodes of around 0.5 nm to the average trace lengths, the values are lower than the ones expected for the fully stretched molecules, see Figure 2c and d, as the inferred values are then still off by roughly a nm in the case of both compounds. A possible explanation relates to the injection and ejection of charge carriers through just a part of the molecule or through the full molecule when mechanically stabilized by parts of the linkers, giving rise to a shorter plateau length than expected for the fully stretched molecule. Indicating also that the conductance of the fully-stretched molecule sits below the noise floor of the used measurement system.

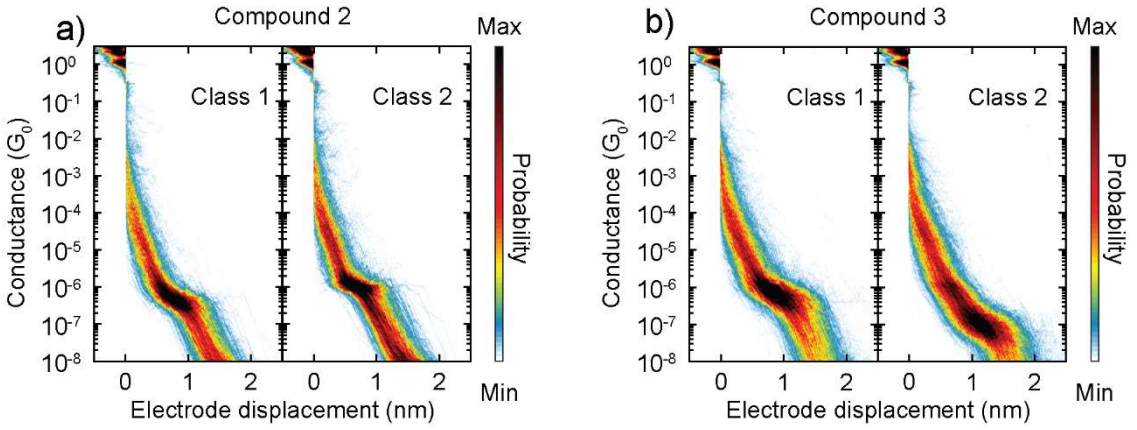


**Figure 7.** Charge transport measurements. (a) Two-dimensional conductance versus electrode displacement histograms displaying two molecular classes (class 1 and 2) for complex **2**. (b) Same as (a) but for compound **3**.

Additional dataset where the reproducibility is studied of complex **3** at 100 mV and the bias dependent charge transport of complex **2** can be found in SI section 8.4. From these additional datasets we neither observe clear differences between different voltages on the charge transport of complex **2**, nor differences amongst datasets using the same bias voltage.

Iron(II) complexes composed of BPP-based ligands are ideal reference systems for studying structure-SCO property relationships, as elaborated by Halcrow and co-workers.[70,75] The parent iron(II)-BPP complex first reported by Halcrow and co-workers in 2001[76] laid the foundation stone for such investigations and several parameters contributing to the occurrence of cooperative SCO in BPP-based complexes have been elucidated. A notable one is the terpyridine embrace packing motif observed in the crystal lattices of some BPP complexes.[77,78] Thermal hysteresis widths in the range of 2 K to 13 K have been reported for complexes following terpyridine embrace- like packing motif in the lattice.[79] A select class of iron(II)-BPP complexes showed thermal hysteresis widths ranging from several tens of kelvin to 100 K.[70,72,80] In such complexes, the HS structure is strongly distorted with respect to the LS structure. Such distortion is quantified by the parameter $\Delta\phi$, the magnitude of it reflects on the severity of distortion. A distorted HS structure need to adopt a less-distorted LS structure to allow the HS to LS switching to proceed. The energetic requirement for such reorganization is substantial considering the constraints imposed by intermolecular interactions in the crystal lattice. Due to this constrain, the HS structure is trapped until sufficient thermal energy is provided, facilitating the HS to LS switching. Other factors contributing to the occurrence of bistable SCO in iron(II)-BPP complexes include steric hindrance imparted by substituents and the consequent conformational orientation, which prevents spin-state conversion at the same temperature. This facet is exemplified for iron(II) complexes $[Fe(COOEt\text{-}BPP)_2(ClO_4)_2]$[72] and $[Fe(F_2\text{-}BPP)_2(ClO_4)_2]$.[75]

Based on the above rationale connecting molecular structure and the nature of SCO in iron(II) BPP complexes, we set out to elucidate the molecular structural origin of bistable SCO observed for complex **1**. Such elucidation for complexes **2** and **3** is rendered impossible due

to the lack of HS structures of the complexes. An inspection of the packing in the crystal lattices of LS and HS forms of complex **1** (Figure S28 and 29) reveals that the molecules pack following a non-terpyridine embrace pattern. Therefore, the contributions from the terpyridine embrace pattern in inducing thermal hysteresis loop in **1** is ruled out. Such conclusion is meaningful considering the presence of 2-ethnylthiophene group in the pyridine ring of complex **1**, prohibiting the close interaction between the BPP-fragments and hence the terpyridine embrace packing. As can be seen in Table 1, the spin-state switching of **1** is accompanied with pronounced variations in angular parameters. We attribute such variations as contributing factors for the occurrence of bi-stable SCO in complex **1**.

Complex **2** presents two interesting cases—the relation between scan rate and thermal hysteresis width and a rarely observed two-step bistable SCO with a stable intermediate spin phase (ISP). Often times, faster scan rates result in wider hysteresis widths for SCO complexes.[34,81,82] Factors such as (i) kinetic lag between the rate of spin-state switching and scan rate and (ii) trapping of a particular spin-state in a metastable state cause the observed scan-rate dependence of thermal hysteresis width. In some systems, spin-state switching is accompanied with large structural phase transitions. At faster scan rates, there is not enough time for the systems to reorient and wide hysteresis widths are observed. The operation of the above mechanisms can be unveiled by performing scan-rate-dependent studies, where slower scan rates result into smaller hysteresis widths. However, for complex **2**, the hysteresis widths obtained at the scan rates of 0.5 K/min and 0.25 K/min are wider than the ones obtained at the scan rates of 1 K/min and above. Such switching behaviour was observed for a mononuclear iron(II) complex—[Fe(*n*Bu-im)$_3$(tren)](PF$_6$)$_2$, where *n*Bu-im and tren stand for 1*H*-imidazol-2-aldehyde and tris(2-ethylamino)amine, respectively.[83] In the complex, fast scanning (4 K/min) resulted in the initialization of the LS1 phase upon HS to LS switching while cooling. On the other hand, slow scanning (0.1 K/min) resulted in the formation of an altogether different LS2 phase. Both the LS1 and LS2 phases switched differently to the same HS state, albeit with different kinetically controlled phase transition. Elucidation of such pathways for **2** is prohibited, unfortunately, by the lack of HS structure and the reproducibility issues.

The two-step SCO with a stable intermediate phase observed for **2** is strikingly reminiscent of the switching observed for [Fe(bapbpy)(NCS)$_2$], bapbpy stands for *N*-(6-(6-(pyridin-2-ylamino)pyridin-2-yl)pyridin-2-yl)pyridin-2-amine, reported by Reedijk and co-workers.[84,85] Cooling of [Fe(bapbpy)(NCS)$_2$] from 300 K resulted in the abrupt and partial HS to LS switching resulting in the formation of an intermediate spin phase with 1:2 HS:LS composition at 231 K. The mixed spin phase is stable in the 231 K to 177 K temperature range. Cooling below 177 K resulted in the switching of remaining HS complexes to LS state. In the heating mode, the stepwise transitions occurred at relatively higher temperatures than the ones observed in the cooling mode constituting a thermal hysteresis loop. Detailed SC-XRD studies revealed that the intermediate spin phase is indeed composed of a distinct HS:LS:LS phase and not a mix of pure HS and LS phases. Such elucidations for complex **2** is rendered impossible due to the lack of molecular structures at different switching temperatures. The crystallization of **2** with lattice acetonitrile solvent and the occurrence of the first irreversible transition well above RT resulted in the disintegration of the crystals upon heating, prohibiting SC-XRD studies at varying switching temperatures. Nevertheless, considering the comparable nature of the

switching profiles observed for **2** and [Fe(bapbpy)(NCS)$_2$], we attribute the intermediate spin phase observed for **2** to a distinct 1:4 HS:LS phase. The above attribution is based on the $\chi T$ = 3.43 cm$^3$mol$^{-1}$K observed for the HS state at 300 K and $\chi T$ = 0.71 cm$^3$mol$^{-1}$K observed in the middle of ISP2 shown in Figure 5b.

The two-step SCO with wide $\Delta T$ observed for **2** is unprecedented, to the best of our knowledge, for iron(II) complexes composed of BPP-based ligands. However, we would like to acknowledge that the switching profile of **2** is not reproducible for a different batch; the exact causes behind such observation is not known at present. However, its worth mentioning that the SCO is sensitive to sample preparation as reported for [Fe(bapbpy)(NCS)$_2$] and its related analogues.[85] Probably, small variations during the crystallization process of **2** and the resultant, albeit small, change in the molecular organization could have caused the different switching profiles observed for batches 1 and 2 of the complex. The crystallization of complexes **1-3** with lattice solvents poses problems as the solvents are expelled from the lattice during the heating process. This leads to concomitant modifications of intermolecular interactions during repeated heat cool cycling, rendering structure spin-state switching property elucidations difficult.

## 3. Conclusions

In this contribution, we have studied three iron(II) complexes—**1-3**—composed of novel BPP-based ligands, each exhibiting distinct switching behaviour. Complexes **1** and **2** showed bistable spin-state switching characteristics. The bistable switching observed for complex **1** is attributed to the involvement of pronounced angular distortion upon spin-state switching. The switching profile of complex **1** is reproducible, although with small differences, across different batches. Complex **2** showed a rarely observed two-step switching process with wide thermal hysteresis widths in both steps. The observation of inverse relation between scan rate and hysteresis width—that is, wider width upon slower temperature scanning—is notable. Unfortunately, the switching profiles observed for complex **2** is not reproducible across batches. Complex **3** showed lattice solvent-dependent spin-state switching and underwent a gradual and incomplete HS to LS switching after the loss of lattice acetonitrile solvent. Single-molecule transport measurements of **2** and **3** reveal charge-transport through part of the molecular segments as a consequence of partially stretched configuration of the complexes in the junctions. Overall, our vision of studying the same complex at the bulk and single-molecule level and elucidation of various interesting mechanistic and application-oriented facets, as discussed in the introduction, are only partially successful due to unforeseen experimental difficulties. The outcomes of our dual-level approach highlight both the opportunities and challenges involved in pursuing SCO complexes for applications.

## Experimental Section

See section S1 and S2 of supporting information for details.

## Supporting Information

Experimental details, synthesis and characterisation of ligands and complexes, crystallographic data of complexes **1-3**, thermo gravimetric analysis data of complexes **1-3**,

spin-state switching studies of complexes **1-3**, and single-molecule transport studies of complexes **2** and **3**.

## Author Contributions

S.K.K.: Conceptualization, Formal analysis, Synthesis and characterization, Magnetic measurements, Writing—original draft; reviewing and editing. S. v. d. P.: Single-molecule transport studies, Formal analysis, Writing—original draft; reviewing and editing. S.S.: Single-crystal X-ray diffraction studies, Writing—reviewing and editing. O. F.: Single-crystal X-ray diffraction studies, Writing—reviewing and editing. H. S. J. v. d. Z.: Writing—reviewing and editing. M. R.: Writing—reviewing and editing.

## Acknowledgements

S.K.K. and M.R. thank the Helmholtz Association for support through the programs Natural, Artificial, and Cognitive Information Processing (NACIP) and Materials Systems Engineering (MSE). The authors thank Karlsruhe Nano Micro Facility (KNMFi) for proving the analytical infrastructure. Karlsruhe Institute of Technology (KIT) library is thanked for covering the Article Processing Charges (APCs) and open access charges through programme DEAL.

## Conflict of Interests

The authors declare no conflict of interests.

## Data Availability Statement

Deposition numbers 2225398 and 2473868 (for **1**), 2194081 (for **2**), and 2210655 (for **3**) contain the supplementary crystallographic data for this paper. These data are provided free of charge by the joint Cambridge Crystallographic Data Centre and Fachinformationszentrum Karlsruhe Access Structures service. All the data are available in the main script and the supporting information.

**Key Words:** Iron(II) complexes · Spin-crossover (SCO)· Bistable switching · Single-molecule transport studies

## References

[1] L. Cambi, L. Szegö, *Ber. dtsch. Chem. Ges. A/B* **1931**, *64*, 2591–2598.
[2] M. A. Halcrow, *Chem. Commun.* **2013**, *49*, 10890.
[3] G. Hörner, B. Weber, *Eur J Inorg Chem* **2024**, *27*, DOI 10.1002/ejic.202400471.
[4] P. Gütlich, Y. Garcia, H. A. Goodwin, *Chem. Soc. Rev.* **2000**, *29*, 419–427.
[5] G. Yang, Z.-P. Ni, M.-L. Tong, *Coordination Chemistry Reviews* **2024**, *521*, 216146.
[6] K. Ridier, A. Hoblos, S. Calvez, M. Lorenc, W. Nicolazzi, S. Cobo, L. Salmon, L. Routaboul, G. Molnár, A. Bousseksou, *Coordination Chemistry Reviews* **2025**, *535*, 216628.
[7] A. Bousseksou, G. Molnár, L. Salmon, W. Nicolazzi, *Chem. Soc. Rev.* **2011**, *40*, 3313.
[8] L. Getzner, Y. Remili, Z. Ziani, L. Vendier, W. Nicolazzi, A. Rotaru, H. Yu, G. Molnár, S. Cobo, A. Bousseksou, *Angew Chem Int Ed* **2025**, DOI 10.1002/anie.202506965.
[9] A. Dürrmann, G. Hörner, D. Baabe, F. W. Heinemann, M. A. C. De Melo, B. Weber, *Nat Commun* **2024**, *15*, DOI 10.1038/s41467-024-51675-1.
[10] P. Gütlich, H. A. Goodwin, D. N. Hendrickson, *Angew. Chem. Int. Ed. Engl.* **1994**, *33*, 425–427.

[11] M. Seredyuk, K. Znovjyak, F. J. Valverde-Muñoz, M. C. Muñoz, T. Delgado, I. Da Silva, J. A. Real, *Inorg. Chem. Front.* **2025**, DOI 10.1039/d5qi00856e.
[12] O. Kahn, *Molecular Magnetism*, Dover Publications, Garden City, New York, **2021**.
[13] E. Coronado, *Nat Rev Mater* **2019**, *5*, 87–104.
[14] O. Kahn, C. J. Martinez, *Science* **1998**, *279*, 44–48.
[15] C. Lefter, V. Davesne, L. Salmon, G. Molnár, P. Demont, A. Rotaru, A. Bousseksou, *Magnetochemistry* **2016**, *2*, 18.
[16] Y. Zhang, R. Torres-Cavanillas, X. Yan, Y. Zeng, M. Jiang, M. Clemente-León, E. Coronado, S. Shi, *Chem. Soc. Rev.* **2024**, *53*, 8764–8789.
[17] M. A. Halcrow, *Polyhedron* **2007**, *26*, 3523–3576.
[18] B. Schäfer, C. Rajnák, I. Šalitroš, O. Fuhr, D. Klar, C. Schmitz-Antoniak, E. Weschke, H. Wende, M. Ruben, *Chem. Commun.* **2013**, *49*, 10986.
[19] L. G. Lavrenova, *J Struct Chem* **2025**, *66*, 803–867.
[20] M. A. Halcrow, *Coordination Chemistry Reviews* **2009**, *253*, 2493–2514.
[21] In *Spin-Crossover Materials*, Wiley, **2013**, pp. 281–301.
[22] G. Chastanet, M. Lorenc, R. Bertoni, C. Desplanches, *Comptes Rendus. Chimie* **2018**, *21*, 1075–1094.
[23] D. Y. Aleshin, I. Nikovskiy, V. V. Novikov, A. V. Polezhaev, E. K. Melnikova, Y. V. Nelyubina, *ACS Omega* **2021**, *6*, 33111–33121.
[24] W. Zhang, R. Alonso-Mori, U. Bergmann, C. Bressler, M. Chollet, A. Galler, W. Gawelda, R. G. Hadt, R. W. Hartsock, T. Kroll, K. S. Kjær, K. Kubiček, H. T. Lemke, H. W. Liang, D. A. Meyer, M. M. Nielsen, C. Purser, J. S. Robinson, E. I. Solomon, Z. Sun, D. Sokaras, T. B. Van Driel, G. Vankó, T.-C. Weng, D. Zhu, K. J. Gaffney, *Nature* **2014**, *509*, 345–348.
[25] Ch. Bressler, C. Milne, V.-T. Pham, A. ElNahhas, R. M. Van Der Veen, W. Gawelda, S. Johnson, P. Beaud, D. Grolimund, M. Kaiser, C. N. Borca, G. Ingold, R. Abela, M. Chergui, *Science* **2009**, *323*, 489–492.
[26] M. Alías-Rodríguez, S. Bhattacharyya, M. Huix-Rotllant, *J. Phys. Chem. Lett.* **2023**, *14*, 8571–8576.
[27] M. Oppermann, F. Zinna, J. Lacour, M. Chergui, *Nat. Chem.* **2022**, *14*, 739–745.
[28] H. T. Lemke, K. S. Kjær, R. Hartsock, T. B. Van Driel, M. Chollet, J. M. Glownia, S. Song, D. Zhu, E. Pace, S. F. Matar, M. M. Nielsen, M. Benfatto, K. J. Gaffney, E. Collet, M. Cammarata, *Nat Commun* **2017**, *8*, DOI 10.1038/ncomms15342.
[29] L. Zhang, K. Ridier, O. Ye. Horniichuk, S. Calvez, L. Salmon, G. Molnár, A. Bousseksou, *J. Phys. Chem. Lett.* **2023**, *14*, 6840–6849.
[30] A. Cannizzo, C. J. Milne, C. Consani, W. Gawelda, Ch. Bressler, F. Van Mourik, M. Chergui, *Coordination Chemistry Reviews* **2010**, *254*, 2677–2686.
[31] R. Bertoni, M. Lorenc, A. Tissot, M. Servol, M. Boillot, E. Collet, *Angew Chem Int Ed* **2012**, *51*, 7485–7489.
[32] M. Bernien, H. Naggert, L. M. Arruda, L. Kipgen, F. Nickel, J. Miguel, C. F. Hermanns, A. Krüger, D. Krüger, E. Schierle, E. Weschke, F. Tuczek, W. Kuch, *ACS Nano* **2015**, *9*, 8960–8966.
[33] Y. Zhang, *The Journal of Chemical Physics* **2020**, *153*, DOI 10.1063/5.0027641.
[34] S. Brooker, *Chem. Soc. Rev.* **2015**, *44*, 2880–2892.
[35] L. Kämmerer, G. Kämmerer, M. Gruber, J. Grunwald, T. Lojewski, L. Mercadier, L. Le Guyader, R. Carley, C. Carinan, N. Gerasimova, D. Hickin, B. E. Van Kuiken, G. Mercurio, M. Teichmann, S. K. Kuppusamy, A. Scherz, M. Ruben, K. Sokolowski-Tinten, A. Eschenlohr, K. Ollefs, C. Schmitz-Antoniak, F. Tuczek, P. Kratzer, U. Bovensiepen, H. Wende, *ACS Nano* **2024**, *18*, 34596–34605.

[36] L. Kipgen, M. Bernien, S. Ossinger, F. Nickel, A. J. Britton, L. M. Arruda, H. Naggert, C. Luo, C. Lotze, H. Ryll, F. Radu, E. Schierle, E. Weschke, F. Tuczek, W. Kuch, *Nat Commun* **2018**, *9*, DOI 10.1038/s41467-018-05399-8.
[37] Y. Jiang, L. C. Liu, A. Sarracini, K. M. Krawczyk, J. S. Wentzell, C. Lu, R. L. Field, S. F. Matar, W. Gawelda, H. M. Müller-Werkmeister, R. J. D. Miller, *Nat Commun* **2020**, *11*, DOI 10.1038/s41467-020-15187-y.
[38] C. Wang, R. Li, X. Chen, R. Wei, L. Zheng, J. Tao, *Angew Chem Int Ed* **2015**, *54*, 1574–1577.
[39] Y. Jiao, J. Zhu, Y. Guo, W. He, Z. Guo, *J. Mater. Chem. C* **2017**, *5*, 5214–5222.
[40] C. Lochenie, K. Schötz, F. Panzer, H. Kurz, B. Maier, F. Puchtler, S. Agarwal, A. Köhler, B. Weber, *J. Am. Chem. Soc.* **2018**, *140*, 700–709.
[41] F.-F. Yan, W.-J. Jiang, N.-T. Yao, P.-D. Mao, L. Zhao, H.-Y. Sun, Y.-S. Meng, T. Liu, *Chem. Sci.* **2023**, *14*, 6936–6942.
[42] I. Jaber El Lala, N. Montenegro-Pohlhammer, R. Sánchez-de-Armas, C. J. Calzado, *Nanoscale* **2025**, *17*, 6141–6153.
[43] T. Miyamachi, M. Gruber, V. Davesne, M. Bowen, S. Boukari, L. Joly, F. Scheurer, G. Rogez, T. K. Yamada, P. Ohresser, E. Beaurepaire, W. Wulfhekel, *Nat Commun* **2012**, *3*, DOI 10.1038/ncomms1940.
[44] G. D. Harzmann, R. Frisenda, H. S. J. Van Der Zant, M. Mayor, *Angew Chem Int Ed* **2015**, *54*, 13425–13430.
[45] S. Johannsen, S. Ossinger, T. Markussen, F. Tuczek, M. Gruber, R. Berndt, *ACS Nano* **2021**, *15*, 11770–11778.
[46] R. Frisenda, G. D. Harzmann, J. A. Celis Gil, J. M. Thijssen, M. Mayor, H. S. J. Van Der Zant, *Nano Lett.* **2016**, *16*, 4733–4737.
[47] T. G. Gopakumar, F. Matino, H. Naggert, A. Bannwarth, F. Tuczek, R. Berndt, *Angew Chem Int Ed* **2012**, *51*, 6262–6266.
[48] C. Yang, Y. Guo, H. Zhang, X. Guo, *Chem. Rev.* **2025**, *125*, 223–293.
[49] E. Burzurí, A. García-Fuente, V. García-Suárez, K. Senthil Kumar, M. Ruben, J. Ferrer, H. S. J. Van Der Zant, *Nanoscale* **2018**, *10*, 7905–7911.
[50] Y. Zhang, S. Giménez-Santamarina, S. Cardona-Serra, F. Gao, E. Coronado, M. Brandbyge, *Nano Lett.* **2024**, *24*, 9846–9853.
[51] S. Pillet, *Journal of Applied Physics* **2021**, *129*, DOI 10.1063/5.0047681.
[52] P. Guionneau, *Dalton Trans.* **2014**, *43*, 382–393.
[53] L. J. Kershaw Cook, R. Mohammed, G. Sherborne, T. D. Roberts, S. Alvarez, M. A. Halcrow, *Coordination Chemistry Reviews* **2015**, *289–290*, 2–12.
[54] M. A. Halcrow, *Chemistry Letters* **2014**, *43*, 1178–1188.
[55] G. Bhatt, A. Ghatak, R. Murugavel, *J Chem Sci* **2023**, *135*, DOI 10.1007/s12039-023-02163-4.
[56] E. Ruiz, *Phys. Chem. Chem. Phys.* **2014**, *16*, 14–22.
[57] D. Aravena, E. Ruiz, *J. Am. Chem. Soc.* **2012**, *134*, 777–779.
[58] M. Gruber, R. Berndt, *Magnetochemistry* **2020**, *6*, 35.
[59] K. S. Kumar, M. Ruben, *Angew Chem Int Ed* **2021**, *60*, 7502–7521.
[60] E. König, K. Madeja, *Chem. Commun. (London)* **1966**, *0*, 61–62.
[61] M. Gruber, V. Davesne, M. Bowen, S. Boukari, E. Beaurepaire, W. Wulfhekel, T. Miyamachi, *Phys. Rev. B* **2014**, *89*, DOI 10.1103/physrevb.89.195415.
[62] J. A. Real, M. C. Muñoz, J. Faus, X. Solans, *Inorg. Chem.* **1997**, *36*, 3008–3013.
[63] T. Palamarciuc, J. C. Oberg, F. El Hallak, C. F. Hirjibehedin, M. Serri, S. Heutz, J.-F. Létard, P. Rosa, *J. Mater. Chem.* **2012**, *22*, 9690.
[64] S. K. Kuppusamy, A. Mizuno, A. García-Fuente, S. Van Der Poel, B. Heinrich, J. Ferrer, H. S. J. Van Der Zant, M. Ruben, *ACS Omega* **2022**, *7*, 13654–13666.
[65] K. Sonogashira, Y. Tohda, N. Hagihara, *Tetrahedron Letters* **1975**, *16*, 4467–4470.

[66] E. Krasnokutskaya, N. Semenischeva, V. Filimonov, P. Knochel, *Synthesis* **2007**, *2007*, 81–84.
[67] M. A. Halcrow, *New J. Chem.* **2014**, *38*, 1868–1882.
[68] K. Senthil Kumar, N. Del Giudice, B. Heinrich, L. Douce, M. Ruben, *Dalton Trans.* **2020**, *49*, 14258–14267.
[69] Y. Oleksii, A. El-Ghayoury, *Molecules* **2025**, *30*, 1314.
[70] I. Capel Berdiell, E. Michaels, O. Q. Munro, M. A. Halcrow, *Inorg. Chem.* **2024**, *63*, 2732–2744.
[71] R. Ketkaew, Y. Tantirungrotechai, P. Harding, G. Chastanet, P. Guionneau, M. Marchivie, D. J. Harding, *Dalton Trans.* **2021**, *50*, 1086–1096.
[72] K. Senthil Kumar, B. Heinrich, S. Vela, E. Moreno-Pineda, C. Bailly, M. Ruben, *Dalton Trans.* **2019**, *48*, 3825–3830.
[73] C. A. Martin, R. H. M. Smit, R. V. Egmond, H. S. J. Van Der Zant, J. M. Van Ruitenbeek, *Review of Scientific Instruments* **2011**, *82*, DOI 10.1063/1.3593100.
[74] D. Cabosart, M. El Abbassi, D. Stefani, R. Frisenda, M. Calame, H. S. J. Van Der Zant, M. L. Perrin, *Applied Physics Letters* **2019**, *114*, DOI 10.1063/1.5089198.
[75] E. Michaels, I. Capel Berdiell, H. B. Vasili, C. M. Pask, M. J. Howard, O. Cespedes, M. A. Halcrow, *Crystal Growth & Design* **2022**, *22*, 6809–6817.
[76] J. M. Holland, C. A. Kilner, M. Thornton-Pett, M. A. Halcrow, J. A. McAllister, Z. Lu, *Chem. Commun.* **2001**, 577–578.
[77] R. Pritchard, C. A. Kilner, M. A. Halcrow, *Chem. Commun.* **2007**, 577–579.
[78] M. A. Halcrow, I. Capel Berdiell, C. M. Pask, R. Kulmaczewski, *Inorg. Chem.* **2019**, *58*, 9811–9821.
[79] A. Ahmed, A. Hall, H. B. Vasili, R. Kulmaczewski, A. N. Kulak, O. Cespedes, C. M. Pask, L. Brammer, T. M. Roseveare, M. A. Halcrow, *Angew Chem Int Ed* **2025**, *64*, DOI 10.1002/anie.202416924.
[80] N. Suryadevara, A. Mizuno, L. Spieker, S. Salamon, S. Sleziona, A. Maas, E. Pollmann, B. Heinrich, M. Schleberger, H. Wende, S. K. Kuppusamy, M. Ruben, *Chemistry A European J* **2022**, *28*, DOI 10.1002/chem.202103853.
[81] H. Kurz, G. Hörner, B. Weber, *Zeitschrift anorg allge chemie* **2021**, *647*, 896–904.
[82] R. Kulmaczewski, J. Olguín, J. A. Kitchen, H. L. C. Feltham, G. N. L. Jameson, J. L. Tallon, S. Brooker, *J. Am. Chem. Soc.* **2014**, *136*, 878–881.
[83] M. Seredyuk, M. C. Muñoz, M. Castro, T. Romero-Morcillo, A. B. Gaspar, J. A. Real, *Chemistry A European J* **2013**, *19*, 6591–6596.
[84] S. Bonnet, M. A. Siegler, J. S. Costa, G. Molnár, A. Bousseksou, A. L. Spek, P. Gamez, J. Reedijk, *Chem. Commun.* **2008**, 5619.
[85] S. Bonnet, G. Molnár, J. Sanchez Costa, M. A. Siegler, A. L. Spek, A. Bousseksou, W.-T. Fu, P. Gamez, J. Reedijk, *Chem. Mater.* **2009**, *21*, 1123–1136.

## Table of Contents

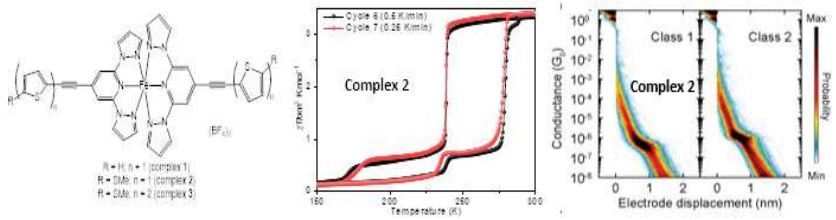


Spin-state switching characteristics of iron(II) complexes—**1**-**3**—composed of functional 2,6-bis(pyrazol-1-yl)pyridine (BPP)-based ligands are presented. Complex **2** shows a remarkable bi-stable switching characteristic, accompanied by a wide thermal hysteresis loop. Single-molecule transport studies of SMe anchoring group tethered complexes **2** and **3** reveal partially stretched configurations and charge transport through segments of molecules.